JOURNAL OF SYNCHROTRON RADIATION

ISSN 1600-5775

Received 10 October 2018
Accepted 21 June 2019

Edited by D. A. Reis, SLAC National Accelerator Laboratory, USA

Keywords: TXM; jitter correction; geometric moment; motion artifact; alignment.

Jitter correction for transmission X-ray microscopy via measurement of geometric moments

Shengxiang Wang,[a,b,c]* Jianhong Liu,[d] Yinghao Li,[c] Jian Chen,[c] Yong Guan[d] and Lei Zhu[c]*

[a]Institute of High Energy Physics, Chinese Academy of Sciences, Beijing 100049, People's Republic of China, [b]Spallation Neutron Source Science Center, Dongguan, Guangdong 523803, People's Republic of China, [c]School of Physical Sciences, University of Science and Technology of China, Hefei, Anhui 230026, People's Republic of China, and [d]National Synchrotron Radiation Laboratory, University of Science and Technology of China, Hefei, Anhui 230026, People's Republic of China. *Correspondence e-mail: wsx231@ustc.edu.cn, leizhusg@ustc.edu.cn

Transmission X-ray microscopes (TXMs) have become one of the most powerful tools for imaging 3D structures of nano-scale samples using the computed tomography (CT) principle. As a major error source, sample jitter caused by mechanical instability of the rotation stage produces shifted 2D projections, from which reconstructed images contain severe motion artifacts. In this paper, a jitter correction algorithm is proposed, that has high accuracy and computational efficiency for TXM experiments with or without nano-particle markers. Geometric moments (GMs) are measured on segmented projections for each angle and fitted to sinusoidal curves in the angular direction. Sample jitter is estimated from the difference between the measured and the fitted GMs for image correction. On a digital phantom, the proposed method removes jitter errors at different noise levels. Physical experiments on chlorella cells show that the proposed GM method achieves better spatial resolution and higher computational efficiency than the re-projection method, a state-of-the-art algorithm using iterative correction. It even outperforms the approach of manual alignment, the current gold standard, on faithfully maintaining fine structures on the CT images. Our method is practically attractive in that it is computationally efficient and lowers experimental costs in current TXM studies without using expensive nano-particles markers.

1. Introduction

Transmission X-ray microscopy (TXM) is one of the most useful technologies in 3D detection on the nanoscale (Wang *et al.*, 2000; Chao *et al.*, 2005; Wang *et al.*, 2016). By providing tomographic images with high spatial resolution, TXM plays an increasingly important role in fundamental research in different fields, including material science (Weker *et al.*, 2014; Nelson *et al.*, 2012), chemistry (Shapiro *et al.*, 2014; Wang, Zhang, *et al.*, 2015) and cell biology (Wang, Wang, *et al.*, 2015; Larabell & Nugent, 2010). A major source of imaging errors in TXM is the sample jitter caused by imperfections of the rotation stage (Wang *et al.*, 2017). In this paper, we propose a practical algorithm to correct sample jitter on the projection images via a rapid alignment technique.

In current practice, TXM uses a stationary storage ring of synchrotron radiation as the X-ray source and a rotating sample stage for projection acquisition. 3D images are reconstructed from 2D parallel projections at different angles according to the computed tomography (CT) imaging principle. Toward a nanoscale spatial resolution, every component in the TXM system requires high mechanical precision and stability. However, the imperfections in the rotation stage,

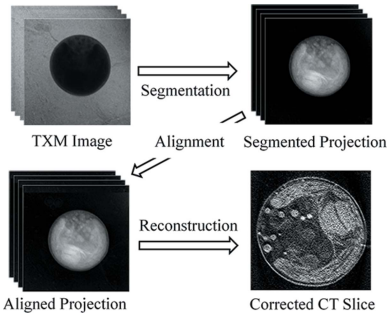

including runout errors, spindle errors and mechanical oscillations, lead to sample jitter during projection acquisition and therefore severe motion artifacts displayed in the reconstructed images (Gürsoy *et al.*, 2017). Jitter correction via projection alignment is an indispensable procedure in current TXM. Many research efforts have been devoted to this topic in the past 20 years, but an optimal solution remains unclear. On current commercial systems, manual alignment is still considered as the most reliable and robust method (Kingston *et al.*, 2011). Nano-particles (*e.g.* gold) are scattered on biological samples to create identifiable markers on projections (Schneider *et al.*, 2002). The locations of the nanoparticles are then manually determined to align the projections for jitter correction. Although it has been shown that automatic tracking algorithms are able to remove the labor-intensive procedure of manual alignment (Cheng *et al.*, 2014), the use of expensive materials for the markers always adds additional cost to the experiments. TXM experiments without markers reduce the complexity and expense of sample preparation while creating extra challenges in signal processing. On marker-less projections, manual alignment becomes infeasible and sophisticated algorithms of jitter correction are required to generate CT images. One popular method iteratively updates the estimation of sample jitter until the corrected projections are consistent with the data acquisition on a stationary sample (Mayo *et al.*, 2007). Each iteration models the X-ray projection process, and the entire computation consists of dozens of re-projections. Long computation time remains the main bottleneck of re-projection-based methods, and research on algorithmic improvements is still ongoing (Gürsoy *et al.*, 2017; Latham *et al.*, 2016).

The center of mass is an intrinsic feature of the sample to be imaged, and can be used in solving different kinds of geometrical problems of the CT system. Hogan *et al.* (1993) used it to remove the translational backlash from projection data. Some reports have used the center of mass to estimate the geometrical parameters of CT systems (Gullberg *et al.*, 1987, 1990). Also, it can be used to compensate movement in CT equipment (Lin, 1994, 1996). However, the center of mass is sensitive to the absorption of the sample, and the accuracy will be affected by beam hardening and scattering. This is not a problem for synchrotron radiation soft X-ray nano-CT, as synchrotron radiation X-rays have a good monochromaticity, and the main interaction of X-rays with matter is via the photoelectric effect at energies lower than 10 keV (Hsieh, 2009). This means that the use of the center of mass has more potential in synchrotron radiation X-ray CT than in medical CT for jitter correction.

In this study, we calculate the jitter errors based on the geometric moments and the principle of CT, and find the best solution that used the center of mass of the sample. Curves of the center of mass versus the projection angle are sinusoidal in the azimuthal direction and constant in the axial direction. Based on this, the proposed method was used on the TXM experiments, and the results verified that this method has high accuracy and computational efficiency for jitter correction in TXM experiments.

2. Method

2.1. Measurement of geometric moments and the proposed jitter correction

TXM uses a parallel beam geometry. If non-idealities (*e.g.* beam hardening effects, scatter *etc.*) of a TXM system are not considered, each projection ray measures a line integral of the linear attenuation coefficients of the scanned sample, written as

$$p_\theta(u, v) = \iiint f(x, y, z)\,\delta(x\cos\theta + y\sin\theta - u, z - v)\,\mathrm{d}x\,\mathrm{d}y\,\mathrm{d}z, \tag{1}$$

where $f(x, y, z)$ is the attenuation function of the sample, $p_\theta(u, v)$ is the projection function at the beam angle θ, and u and v are the horizontal and vertical positions of the projection.

As the jitter errors occur in the u and v directions of the sample projection, the geometric moments can be written as

$$mu_s(\theta) = \iint u^s p_\theta(u, v)\,\mathrm{d}u\,\mathrm{d}v \tag{2}$$

and

$$mv_s(\theta) = \iint v^s p_\theta(u, v)\,\mathrm{d}u\,\mathrm{d}v \tag{3}$$

in the u and v directions, respectively, where s is a non-negative integer, representing the order of the moment.

Based on equation (1), equations (2) and (3) become

$$mu_s(\theta) = \iiint (x\cos\theta + y\sin\theta)^s f(x, y, z)\,\mathrm{d}x\,\mathrm{d}y\,\mathrm{d}z \tag{4}$$

and

$$mv_s(\theta) = \iiint z^s f(x, y, z)\,\mathrm{d}x\,\mathrm{d}y\,\mathrm{d}z. \tag{5}$$

Denoting u_θ and v_θ as the jitters of the projection image at angle θ, $mu_s(\theta)'$ and $mv_s(\theta)'$ are the geometric moments (GMs) of the jitter projections in the u and v directions, respectively. Based on equations (2) and (3), we have

$$mu_s(\theta)' = \iint (u + u_\theta)^s p_\theta(u, v)\,\mathrm{d}u\,\mathrm{d}v, \tag{6}$$

$$mv_s(\theta)' = \iint \left(v + v_\theta\right)^s p_\theta(u, v)\,\mathrm{d}u\,\mathrm{d}v. \tag{7}$$

Thus, we can derive, when $s = 1$,

$$u_\theta = \frac{mu_1(\theta)'}{mu_0(\theta)} - \frac{mu_1(\theta)}{mu_0(\theta)}, \qquad v_\theta = \frac{mv_1(\theta)'}{mv_0(\theta)} - \frac{mv_1(\theta)}{mv_0(\theta)}, \tag{8}$$

and, when $s = 2$,

$$\begin{aligned} u_\theta &= \left(\frac{mu_1(\theta)^2}{mu_0(\theta)^2} - \frac{mu_2(\theta)}{mu_0(\theta)} + \frac{mu_2(\theta)'}{mu_0(\theta)}\right)^{1/2} - \frac{mu_1(\theta)}{mu_0(\theta)} \\ &= \frac{mu_1(\theta)'}{mu_0(\theta)} - \frac{mu_1(\theta)}{mu_0(\theta)}, \\ v_\theta &= \left(\frac{mv_1(\theta)^2}{mv_0(\theta)^2} - \frac{mv_2(\theta)}{mv_0(\theta)} + \frac{mv_2(\theta)'}{mv_0(\theta)}\right)^{1/2} - \frac{mv_1(\theta)}{mv_0(\theta)} \\ &= \frac{mv_1(\theta)'}{mv_0(\theta)} - \frac{mv_1(\theta)}{mv_0(\theta)}, \end{aligned} \tag{9}$$

where $mu_0(\theta) = mv_0(\theta) = \iiint f(x, y, z)\,dx\,dy\,dz$ is the mass of the sample, and $mu_i(\theta)$ and $mv_i(\theta)$ ($i = 1$ or 2) are GMs without shifts.

As the definite integral of the attenuation function $f(x, y, z)$ is a constant, it can be easily certified that $mu_1(\theta)/mu_0(\theta)$ is a sinusoidal curve based on equation (4), and $mv_1(\theta)/mv_0(\theta)$ is a constant based on equation (5). In order to calculate u_θ and v_θ of the projection image, the sinusoidal curve $mu_1(\theta)/mu_0(\theta)$ can be acquired by fitting $mu_1(\theta)'/mu_0(\theta)$ using the least-squares method. We denote $mu_1(\theta)_f$ as the fitted sinusoidal curve based on $mu_1(\theta)'$, and $mv_1(\theta)_f$ as the constant fitted by $mv_1(\theta)'$. Considering the detector offset in the reconstruction, u_θ can be written as

$$u_\theta = \frac{mu_1(\theta)'}{mu_0(\theta)} - \frac{mu_1(\theta)_f}{mu_0(\theta)} - \left(\frac{w}{2} - \frac{\overline{mu_1(\theta)_f}}{mu_0(\theta)}\right), \tag{10}$$

and, for the harmonization of reconstructed slices, v_θ is defined as

$$\begin{aligned} v_\theta &= \frac{mv_1(\theta)'}{mv_0(\theta)} - \frac{mv_1(\theta)_f}{mv_0(\theta)} - \left(\frac{h}{2} - \frac{mv_1(\theta)_f}{mv_0(\theta)}\right) \\ &= \frac{mv_1(\theta)'}{mv_0(\theta)} - \frac{h}{2}, \end{aligned} \tag{11}$$

where w and h are the width and height of the detector, respectively, and $\overline{mu}_1(\theta)_f/mu_0(\theta)$ are the mean values of $mu_1(\theta)_f/mu_0(\theta)$.

The fitted sine curve, $f(\theta)$, can be written as

$$f(\theta) = a + b\cos(\omega\theta) + c\sin(\omega\theta), \tag{12}$$

where $\omega = 2\pi/360$ when we acquire the projections every 1° in the simulation and practical experiments, and we have

$$\begin{bmatrix} 1 & \cos(\omega\theta_1) & \sin(\omega\theta_1) \\ 1 & \cos(\omega\theta_2) & \sin(\omega\theta_2) \\ . & . & . \\ . & . & . \\ 1 & \cos(\omega\theta_m) & \sin(\omega\theta_m) \end{bmatrix} \begin{bmatrix} a \\ b \\ c \end{bmatrix} = \begin{bmatrix} f(\theta_1) \\ f(\theta_2) \\ . \\ . \\ f(\theta_m) \end{bmatrix}, \tag{13}$$

where m is the number of projections. Let $\boldsymbol{\lambda} = [a, b, c]^T$, $\mathbf{A} = [f(\theta_1), f(\theta_2), \ldots, f(\theta_m)]$ and

$$\boldsymbol{\eta} = \begin{bmatrix} 1 & \cos(\omega\theta_1) & \sin(\omega\theta_1) \\ 1 & \cos(\omega\theta_2) & \sin(\omega\theta_2) \\ . & . & . \\ . & . & . \\ 1 & \cos(\omega\theta_m) & \sin(\omega\theta_m) \end{bmatrix}.$$

Equation (13) can be rewritten in the matrix form

$$\mathbf{A} = \boldsymbol{\eta}\boldsymbol{\lambda}, \tag{14}$$

and $\boldsymbol{\lambda}$ can be calculated through the least-squares method (Zeng *et al.*, 1995; Reutter *et al.*, 2000),

$$\boldsymbol{\lambda} = \left(\boldsymbol{\eta}^T\boldsymbol{\eta}\right)^{-1}\boldsymbol{\eta}^T\mathbf{A}. \tag{15}$$

The higher-order GMs can also be used in theory. However, the solutions of high-order GMs with noise will increase the errors greatly, and the fitting curve will consist of the nth power ($n > 1$) of $\sin\theta$, which is also sensitive to the errors. So we are free to find any solutions of high-order moments here.

2.2. Evaluation

Chlorella cells with and without labeled fluorescent nanoparticles are also used as experimental subjects in this study. All the experiments are accomplished by using the soft X-ray microscope at beamline BL07W (Liu *et al.*, 2018) of the National Synchrotron Radiation Laboratory (NSRL) in Hefei, China. A traditional 100-mesh transmission electron microscopy (TEM) grid is used here to hold the cells. Before moving the grid to the rotation stage, an important step is the rapid freezing of the sample with liquid nitrogen, which can help fix the cell well and suppress the damage of radiation to cellular structures. The X-ray energy used in the experiments is 520 eV. A series of sequential projection images are recorded from −60° to 60° with a 1° increment and an exposure time of 5 s for each projection. The size of each projection is 950 × 950 pixels with a pixel size of 11.8 nm × 11.8 nm. The proposed jitter correction method is implemented in Matlab R2014a on a 3.40 GHz eight-core PC. The processing of one experimental dataset typically takes about 15 s.

The transmission X-ray microscopy sample, a chlorella cell, is immobilized inside an ice cube in all experiments, in the so-called 'water window' (McDermott *et al.*, 2009). Photons within this energy range are absorbed an order of magnitude more strongly by carbon- and nitrogen-containing organic material than by water. However, in order to calculate the GM of the chlorella accurately, a threshold-based image segmentation algorithm (Eidheim *et al.*, 2004) is used to segment the cell. The values of the areas surrounding the chlorella are changed to zeros as we are calculating the GM characteristic parameters of chlorella only. The workflow of the process is shown in Fig. 1.

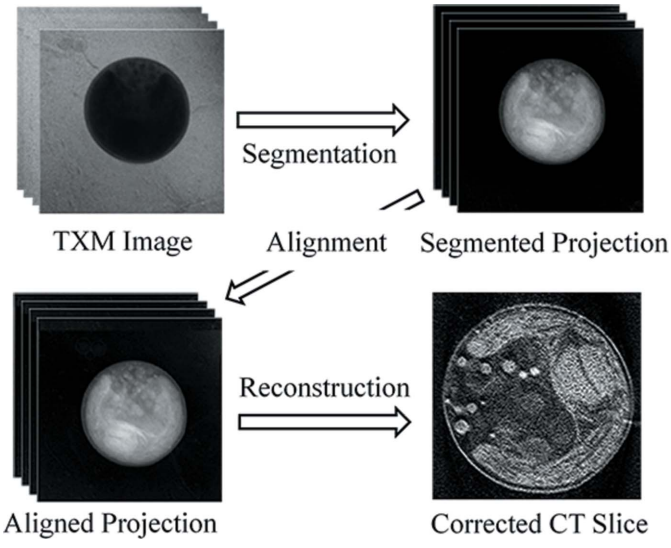

Figure 1
Workflow of the proposed jitter correction.

For the case of chlorella with labeled nano-particles, as X-rays pass through some of the labeled nano-particles together with the chlorella to the detector, these nano-particles will also absorb X-rays and introduce errors to the calculated GM of chlorella. The GM of chlorella is no longer precise enough to perform jitter correction, so instead the GMs of the nano-particles are calculated for the alignment of projections with jitter errors. As it is difficult to track the same nano-particle accurately (Schonberger & Frahm, 2016) from different projections with shifts, we use the GM-based method of segmented chlorella to perform a coarse jitter correction at first, and then a fine correction can be carried out by using the GMs of the nano-particles.

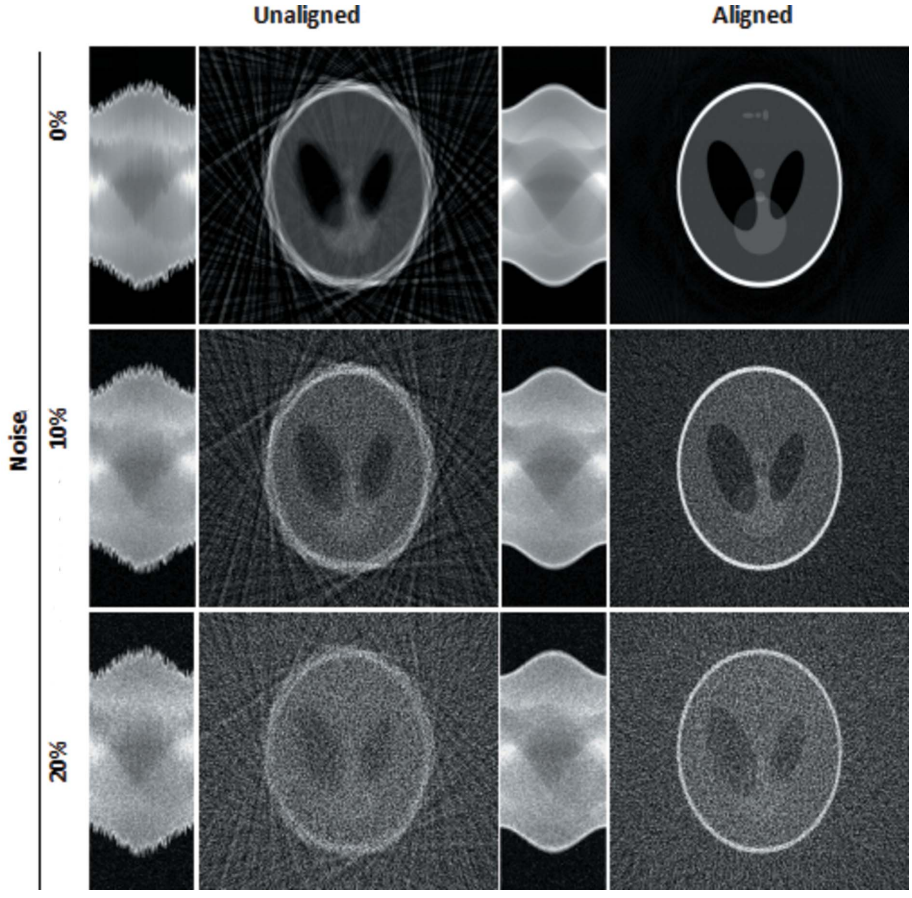

Figure 2
Sinograms and reconstructed slices of the Shepp–Logan phantom study at different noise levels (0%, 10% and 20%). Display windows: sinogram [0 1.2], reconstructed slice [0 0.01].

3. Results and discussion

3.1. Digital phantom study

We first use the digital Shepp–Logan phantom as the sample for method evaluation. The setting of parameters in projection acquisition and image reconstruction mimics that of the TXM system used in our physical experiments, except that projections with no missing angles are simulated to investigate the effect of jitter correction in the absence of CT image artifacts of limited angles. 360 equiangular projections over 360° are simulated for a CT scan with a parallel geometry, and each projection has a size of 512 × 512 pixels. The rotational axis is in the direction of the y-axis, the direction of X-ray propagation is defined as being along the z-axis, and the x-axis is perpendicular to the y–z plane, which is the same for the experimental data. Random jitter errors of a standard uniform distribution over a ± 10 pixels range along the x- and y-axis were performed for each projection.

Three levels of Poisson noise (0%, 10% and 20%) were considered in evaluating the algorithm robustness, and the jitter errors were calculated by using the proposed method. All the jitter errors calculated were equal to the ground truth even for high levels of noise up to 20%, and the sinograms and reconstructed slices with and without correction are shown in Fig. 2.

3.2. Chlorella experiment without nano-particle markers

Fig. 3 shows sinograms and reconstructed slices of the chlorella cell, in order to clearly display the reconstructed results of different methods; not only the reconstructed slices in the x–y plane but also the slices in the x–z plane are shown in the figure.

Fig. 3(a1) is a sinogram of raw data acquired from the TXM experiment which has jitter errors. Figs. 3(a2)–3(a3) are the reconstructed slices with motion artifacts. The TXM operating system (Xradia) provides a manual correction method, which needs the laboratorian to align the projections with a feature point image by image. Two small spherical subcellular structures are selected to perform the jitter correction. Fig. 3(b1) shows the sinogram after manual alignment on the Xradia operating system. Because the points used here are either large or have low contrast, jitter errors are still obvious after alignment, which leads to inaccurate structural results. Even so, the reconstructed images reveal more information than the images before alignment. Fig. 3(c1) is the corresponding sinogram after 30 iterations of re-projection alignment, which becomes continuous and smooth. Figs. 3(c2) and 3(c3) are reconstructed slices after alignment. The organelles are clearly revealed in the x–z plane [Fig. 3(c3)], for example, the cytomembrane, nuclear membranes, starch sheath, lipid droplets and some other subcellular structures. However, the slice in the x–y plane [Fig. 3(c2)] is poorly reconstructed. Figs. 3(d1)–3(d3) are results after GM alignment. When comparing the limited angle results in the x–y plane, it is obvious that the GM method provides the best result among the four slices as it is

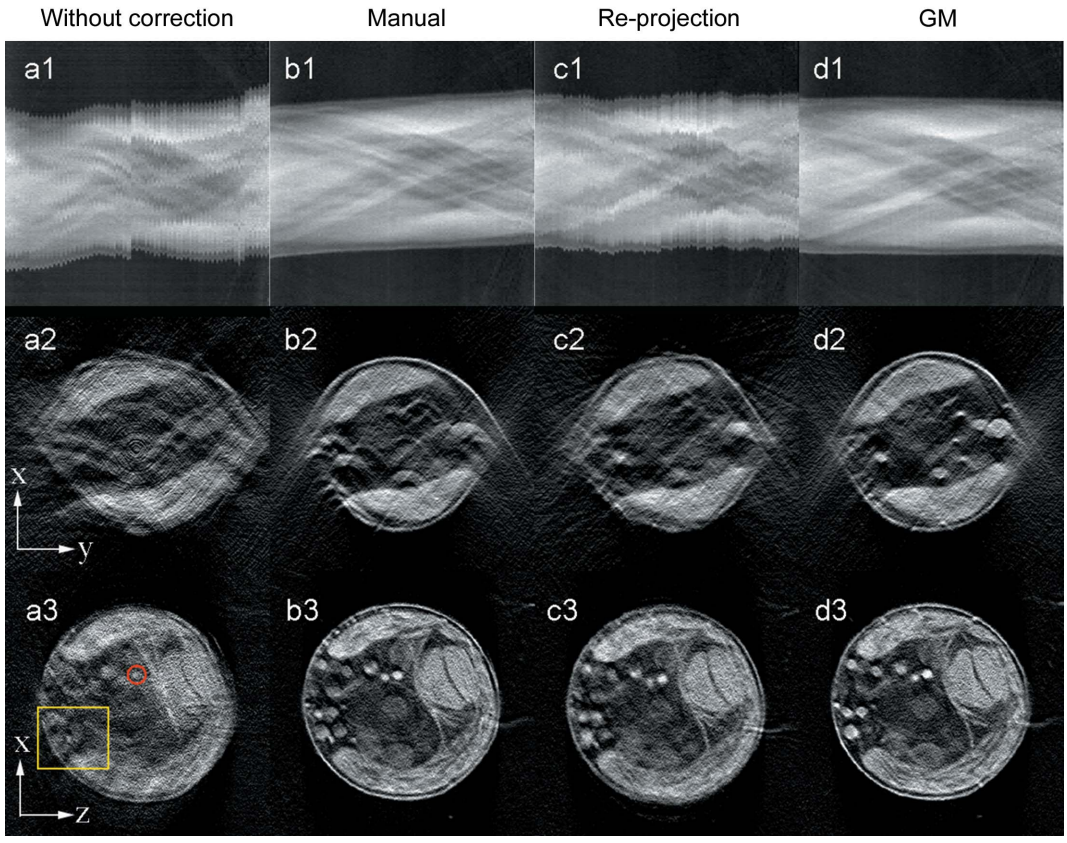

Figure 3
Sinograms (top row) and reconstructed slices of a chlorella cell using different methods. Row 2: reconstructed slices of row 1, displayed in the *x*–*y* plane. Row 3: reconstructed slices in the *x*–*z* plane. Columns from (*a*) to (*d*) are results of TXM without jitter correction, corrected by a re-projection based method (Mayo *et al.*, 2007), by manual alignment and by the proposed GM method. Display windows: [0 0.015] μm^{-1}.

well known that most of the subcellular structures are spherical in chlorella. When comparing the slices in the *x*–*z* plane, we find that Fig. 3(*c*3) has more substructures than Fig. 3(*d*3) in the region marked by the yellow square; however, because of the mis-aligned result of Fig. 3(*c*2), we can infer that some substructures of Fig. 3(*c*3) are ghosts in the *y*-direction; at the same time, well bounded substructures in Fig. 3(*d*3) appear to be more reasonable.

For a quantitative analysis of the reconstructed slices using different methods, we chose a point as the center of circle and calculated the mean values of the circular regions for increasing radius. All the mean values of the concentric circles with radius from 4 to 13 pixels were used to draw a characteristic curve to analyze the results. The region shown by the red circle in row 3 of Fig. 3 in the reconstructed results was chosen. Fig. 4 shows comparison results for the four different reconstruction results. The mean values of the first circular regions of the four slices are normalized. The end values at a radius of 13 pixels are 0.6103, 0.4273, 0.4019 and 0.3710 from top to bottom in Fig. 4. The result shows that the GM alignment method provides the most rapid curve and highest contrast, along with the re-projection alignment, manual alignment methods and the result without correction. This means that the GM method achieves a better spatial resolution and contrast than the manual alignment and re-projection method. Finally, time cost of the manual method is about 20 min, the computing time of the re-projection method is about 2 h, but the proposed method takes only about 30 s to carry out the jitter correction.

3.3. Chlorella with labeled nano-particles

Labeled nano-particles are always used as feature points in TXM experiments so that the manual alignment method can

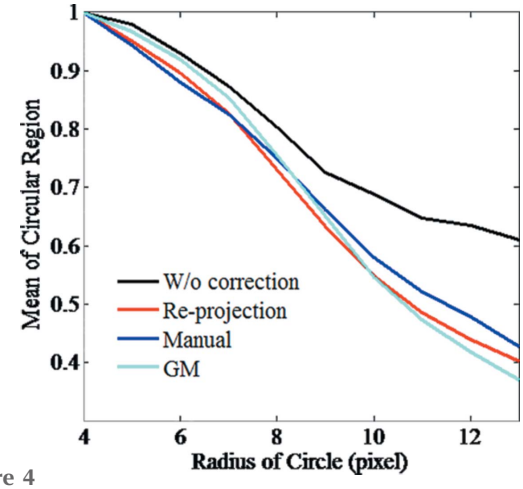

Figure 4
Comparison of four different reconstruction results with mean values curves of the regions in the red circles in Fig. 3.

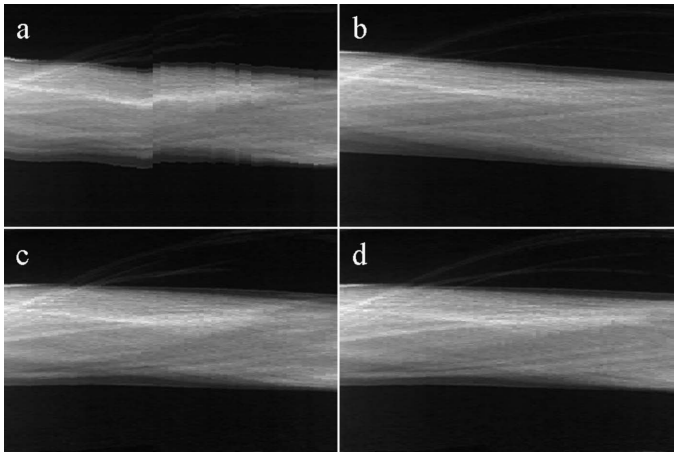

Figure 5
Sinograms of chlorella projections with labeled nano-particles. (*a*) Sinogram of raw data. (*b*) Sinogram after jitter correction with manual alignment. (*c*, *d*) Sinograms after coarse (*c*) and fine (*d*) correction with GM alignment.

be used to correct jitter errors accurately, which is a good control group for verifying the proposed method. As X-rays penetrate the chlorella with some of the particles at partial angles, those nano-particles will absorb X-rays and introduce errors to the calculated GM of the cell, so it is unsatisfactory to use the GM-based method for a cell when it is surrounded by a lot of marked particles.

In this situation, two step corrections are necessary. The first step is a coarse correction based on the segmented chlorella; after that, most of the jitters are compensated [Fig. 5(*c*)], but small jitter errors still exist in the projections. The second step is a fine correction based on the nano-particles. This operation can solve the residual small jitters in the first step; the curves in the upper part of Fig. 5(*d*) are particles after jitter correction.

Fig. 6 shows reconstructed slices of chlorella with labeled nano-particles using different alignment methods. Column (*b*) shows reconstructed slices after manual alignment; the prolonged period of intensive work has also yielded good CT

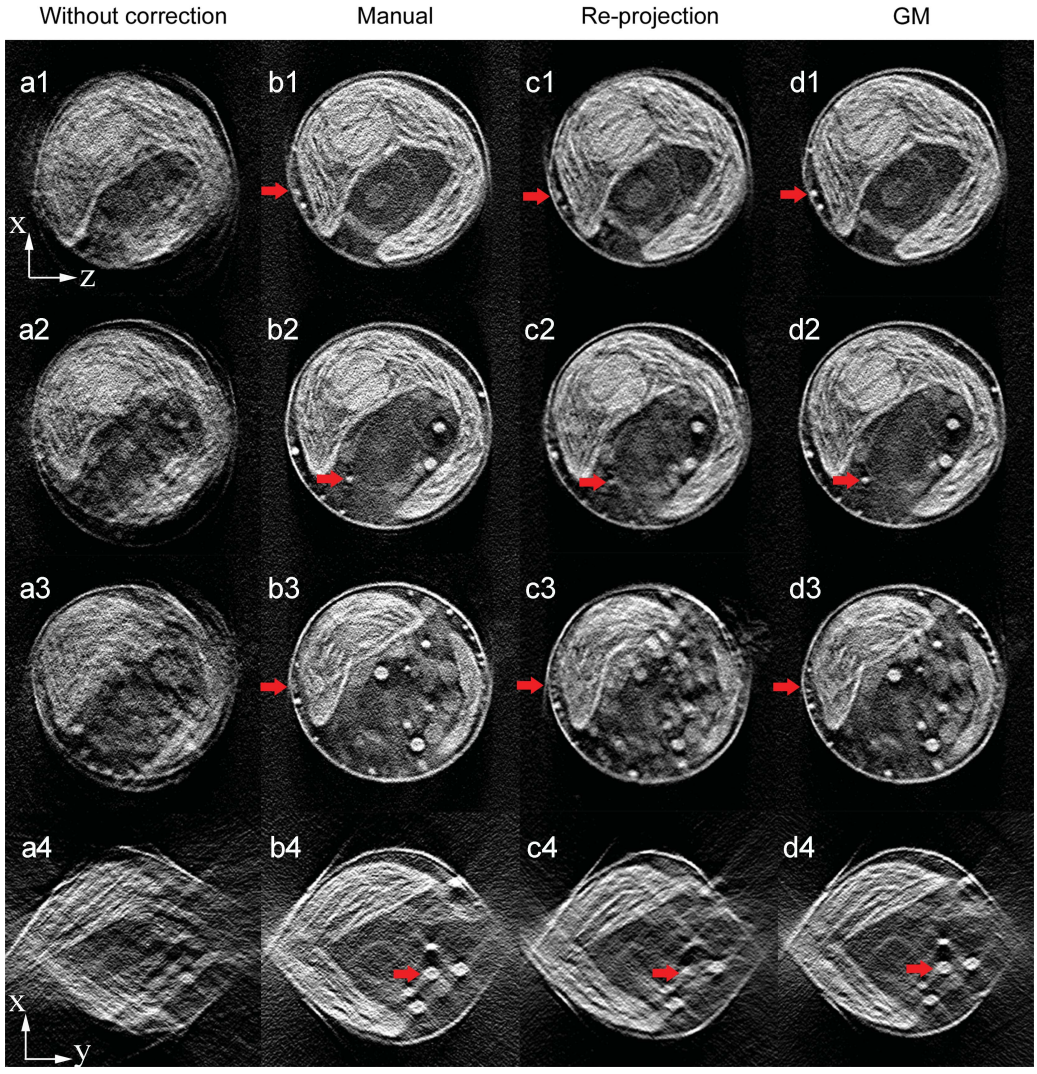

Figure 6
Reconstructed slices of chlorella using different align methods. Columns (*a*) to (*d*) are slices of raw data, after using GM, re-projection and manual alignment. Rows 1 to 3 are reconstructed slices from the *x*–*z* plane, with uniform spaced distance of 50 pixels in the *y* direction. Row 4 are reconstructed slices in the *x*–*z* plane. Display window: [0 0.02] μm^{-1}.

results, as the cytomembrane, starch sheath, lipid droplets and some other subcellular structures can be seen clearly. Column (*c*) shows reconstructed slices of chlorella with re-projection correction; some of the slices seem to show good results after alignment, but the slice in (*c*3) shows many blurred substructures. Column (*d*) shows slices after jitter correction using GM alignment; the substructures are clearly revealed in the slices. Red arrows in Fig. 6 point to the following structure details: (*d*1)–(*d*2) have sharper circular structure than (*b*1)–(*b*2) and (*c*1)–(*c*2); the contour of the cell should be a complete circle, (*d*3) has a relatively good result, but (*b*3) and (*c*3) have a slight dislocation between the upper part and the lower part of the cell; (*b*4) and (*d*4) provide clearer substructures than (*c*4) in the *x*–*y* plane. Finally, the computing time of the proposed method is about 180 s.

4. Conclusions

We propose an accurate and efficient method for jitter correction in TXM. The GM-based method can be used for alignment of a mark-less sample and provides accurate results with better spatial resolution and contrast than re-projection and manual alignment methods. However, it should be noted that a higher number of impurities surrounding the sample will introduce more errors to the calculation of the GM characteristics points of the sample; at the same time, the sample should be completely in the field of view.

For the sample surrounded by markers, nano-particles are regarded as targets when using the GM method for jitter correction. Segmented chlorellas of projection images based on the GM method are used to perform a coarse correction of jitter errors first, and a refined correction on the nano-particles using the GM method is performed thereafter. Considering the usefulness of several different approaches, we are more interested in the data that cannot be corrected by using traditional manual alignment. Above all, the proposed method can complete the jitter correction in tens of seconds, which can improve research efficiency and save experiment costs. At the same time, we believe that the alignment method proposed here can also be used in some other tomography technologies, for example, X-ray fluorescence and electron microscopy.

Acknowledgements

The authors have no relevant conflicts of interest to disclose.

Funding information

The following funding is acknowledged: National Natural Science Foundation of China (grant No. 81671681); China Postdoctoral Science Foundation (grant No. 2018M632551); Fundamental Research Funds for the Central Universities (grant No. WK2030040089; grant No. WK2030040093); Ministry of Science and Technology of China Key Research and Development Projects (grant No. 2016YFC0101400).

References

Chao, W., Harteneck, B. D., Liddle, J. A., Anderson, E. H. & Attwood, D. T. (2005). *Nature*, **435**, 1210–1213.
Cheng, C. C., Chien, C. C., Chen, H. H., Hwu, Y. & Ching, Y. T. (2014). *PLoS One*, **9**, e84675.
Eidheim, O. C., Aurdal, L., Omholt-Jensen, T., Mala, T. & Edwin, B. (2004). *Int. Congr. Ser.* **1268**, 201–206.
Gullberg, G. T., Tsui, B. M. W., Crawford, C. R., Ballard, J. G. & Hagius, J. T. (1990). *Med. Phys.* **17**, 264–272.
Gullberg, G. T., Tsui, B. M. W., Crawford, C. R. & Edgerton, E. R. (1987). *Phys. Med. Biol.* **32**, 1581–1594.
Gürsoy, D., Hong, Y. P., He, K., Hujsak, K., Yoo, S., Chen, S., Li, Y., Ge, M., Miller, L. M., Chu, Y. S., De Andrade, V., He, K., Cossairt, O., Katsaggelos, A. K. & Jacobsen, C. (2017). *Sci. Rep.* **7**, 11818.
Hogan, J. P., Gonsalves, R. A. & Krieger, A. S. (1993). *IEEE Trans. Nucl. Sci.* **40**, 1238–1241.
Hsieh, J. (2009). *Computed Tomography: Principles, Design, Artifacts, and Recent Advances.* Bellingham, WA: SPIE.
Kingston, A., Sakellariou, A., Varslot, T., Myers, G. & Sheppard, A. (2011). *Med. Phys.* **38**, 4934–4945.
Larabell, C. A. & Nugent, K. A. (2010). *Curr. Opin. Struct. Biol.* **20**, 623–631.
Latham, S. J., Kingston, A. M., Recur, B., Myers, G. R. & Sheppard, A. P. (2016). *Proc. SPIE*, **9967**, 996710.
Lin, W. T. (1994). *Proc. SPIE*, **2167**, 743–755.
Lin, W. T. (1996). US Patent 5579358.
Liu, J., Li, F., Chen, L., Guan, Y., Tian, L., Xiong, Y., Liu, G. & Tian, Y. (2018). *J. Microsc.* **270**, 64–70.
Mayo, S., Miller, P., Gao, D. & Sheffield-Parker, J. (2007). *J. Microsc.* **228**, 257–263.
McDermott, G., Le Gros, M. A., Knoechel, C. G., Uchida, M. & Larabell, C. A. (2009). *Trends Cell Biol.* **19**, 587–595.
Nelson, J., Misra, S., Yang, Y., Jackson, A., Liu, Y., Wang, H., Dai, H., Andrews, J. C., Cui, Y. & Toney, M. F. (2012). *J. Am. Chem. Soc.* **134**, 6337–6343.
Reutter, B. W., Gullberg, G. T. & Huesman, R. H. (2000). *IEEE Trans. Med. Imaging*, **19**, 434–450.
Schneider, G., Anderson, E., Vogt, S., Knöchel, C., Weiss, D., Legros, M. & Larabell, C. (2002). *Surf. Rev. Lett.* **09**, 177–183.
Schonberger, J. L. & Frahm, J. M. (2016). *Proceedings of the IEEE Conference on Computer Vision and Pattern Recognition (CVPR-2016)*, pp. 4104–4113.
Shapiro, D. A., Yu, Y.-S., Tyliszczak, T., Cabana, J., Celestre, R., Chao, W., Kaznatcheev, K., Kilcoyne, A. L. D., Maia, F., Marchesini, S., Meng, Y. S., Warwick, T., Yang, L. L. & Padmore, H. (2014). *Nat. Photon.* **8**, 765–769
Wang, C. C., Chiang, C. C., Liang, B., Yin, G. C., Weng, Y. T. & Wang, L. C. (2017). *Sci. Rep.* **7**, 3691.
Wang, L., Zhang, T., Li, P., Huang, W., Tang, J., Wang, P., Liu, J., Yuan, Q., Bai, R., Li, B., Zhang, K., Zhao, Y. & Chen, C. (2015). *ACS Nano*, **9**, 6532–6547.
Wang, P., Lombi, E., Zhao, F. J. & Kopittke, P. M. (2016). *Trends Plant Sci.* **21**, 699–712.
Wang, S., Wang, D., Wu, Q., Gao, K., Wang, Z. & Wu, Z. (2015). *J. Synchrotron Rad.* **22**, 1091–1095.
Wang, Y., Jacobsen, C., Maser, J. & Osanna, A. (2000). *J. Microsc.* **197**, 80–93.
Weker, J. N., Liu, N., Misra, S., Andrews, J. C., Cui, Y. & Toney, M. F. (2014). *Energy Environ. Sci.* **7**, 2771–2777.
Zeng, G. L., Gullberg, G. T. & Huesman, R. H. (1995). *IEEE Trans. Nucl. Sci.* **42**, 2339–2346.